How does the phytoplankton-light feedback affect the marine N_2O inventory?

Sarah Berthet [1*], Julien Jouanno [2], Roland Séférian [1], Marion Gehlen [3], William Llovel [4]

[1] CNRM, Université de Toulouse, Météo-France, CNRS, Toulouse, France
[2] LEGOS, Université de Toulouse, IRD, CNRS, CNES, UPS, Toulouse, France
[3] LSCE, Université Paris-Saclay, Institut Pierre Simon Laplace, Gif-Sur-Yvette, France
[4] LOPS, CNRS/University of Brest/IFREMER/IRD, Brest, France

([*]correspondence: sarah.berthet@meteo.fr)

Abstract

The phytoplankton-light feedback (PLF) describes the interaction between phytoplankton biomass and the downwelling shortwave radiation entering the ocean. The PLF allows to simulate differential heating across the ocean water column as a function of phytoplankton concentration. Only one third of the Earth system models contributing to the 6th phase of the Coupled Model Intercomparison Project (CMIP6) includes a complete representation of the PLF. In other models, the PLF is approximated either by a prescribed climatology of chlorophyll or not represented at all. Consequences of an incomplete representation of the PLF on the modelled biogeochemical state have not yet been fully assessed and remain a source of multi-model uncertainty in future projection. Here, we evaluate within a coherent modelling framework how representations of the PLF of varying complexity impact ocean physics and ultimately marine production of nitrous oxide (N_2O), a major greenhouse gas. We exploit global sensitivity simulations at 1-degree of horizontal resolution over the last two decades (1999-2018) coupling ocean, sea ice and marine biogeochemistry. The representation of the PLF impacts ocean heat uptake and temperature of the first 300 meters of the tropical ocean. Temperature anomalies due to an incomplete PLF representation drive perturbations of ocean stratification, dynamics and oxygen concentration. These perturbations translate into different projection pathways for N_2O production depending on the choice of the PLF representation. The oxygen concentration in the North Pacific oxygen minimum zone is overestimated in model runs with an incomplete representation of the PLF which results in an underestimation of local N_2O production. This leads to important regional differences of sea-to-air N_2O fluxes: fluxes are enhanced by up to 24% in the south Pacific and south Atlantic subtropical gyres, but reduced by up to 12% in oxygen minimum zones of the northern hemisphere. Our results based on a global ocean-biogeochemical model at CMIP6 state-of-the-art shed light on current uncertainties in modelled marine nitrous oxide budgets in climate models.

Plain language summary

Phytoplankton absorbs the solar radiation entering the ocean surface, and contributes to keep the associated energy in surface waters. This natural effect is either not represented in the ocean component of climate models, or in a simplified manner. We show that an incomplete representation of this biophysical interaction affects the way climate models simulate ocean warming, which leads to uncertainties in projections of oceanic emissions of an important greenhouse gas called the nitrous oxide.

Key points:
- forced ocean-biogeochemical simulations reveal that marine production of nitrous oxide is sensitive to the representation of the phytoplankton-light feedback
- the phytoplankton-light feedback perturbs the accumulation of heat and the ocean dynamics which drive changes in nitrous oxide production patterns
- an incomplete phytoplankton-light feedback overestimates sea-to-air N$_2$O fluxes by up to 24% in subtropical gyres and reduces them by up to 12% in oxygen minimum zones

1. Introduction

Feedbacks between the physical, biogeochemical, or ecosystem components of the ocean can trigger abrupt system changes (Heinze et al., 2021). At present the interactive phytoplankton-light feedback (PLF) is the only coupling in Earth system models between modelled marine biogeochemistry and ocean dynamics (Séférian et al., 2020). It implies that the chlorophyll (CHL) produced by the biogeochemical model is used to determine the fraction of shortwave radiation penetrating ocean surface waters. In this case, the CHL concentration profile used to approximate the influence of plankton biomass on the vertical redistribution of heat in the upper ocean is consistent with the one used to compute biogeochemical cycling.

a) Phytoplankton-light feedback (PLF)

Since the first observational evidence on how suspended matter in surface waters will impact light absorption by the ocean and change the radiative imbalance within the mixed layer (Kahru et al. 1993), this biophysical interaction has been gradually included to ocean models. Gildor and Naik (2005) highlighted the importance of considering monthly variations of CHL to capture the first-order effect of marine biota on light penetration in ocean models. Adding light-CHL interactions to numerical simulations affected oceanic processes over a wide range of spatial and temporal scales. Enabling a phytoplankton-light interaction modifies the hydrodynamics of the water column (Edwards et al., 2001; Edwards et al., 2004), the intensity of the spring-bloom in subpolar regions (Oschlies, 2004), the maintenance of the Pacific Cold Tongue (Anderson et al., 2007), the seasonality of the Arctic Ocean (Lengaigne et al., 2009), the strength of the tropical Pacific annual cycle, as well as the ENSO variability (Timmermann and Jin, 2002; Marzeion et al., 2005), the northward extension of the meridional overturning circulation (Patara et al., 2012) and the cooling of the Atlantic and Peru-Chili upwelling systems (Hernandez et al., 2017, Echevin et al., 2022).

However, the mean effect of the PLF on sea surface temperature has been argued to depend on the numerical framework (forced ocean versus coupled ocean-atmosphere models). The conflicting results reported in the literature were mainly due to diverging bio-optical protocols among models rather than to the inclusion of air-sea coupling. According to Park et al. (2014) atmosphere-ocean coupling amplifies the mean of PLF-induced changes, but without altering the sign of the response obtained in ocean-only simulations. Two main causes were put forward

to explain the sign of the final heat perturbation: either an indirect dynamical response (Murtugudde et al., 2002; Löptien et al., 2009) or a direct thermal effect (Mignot et al., 2013; Hernandez et al., 2017). Hernandez et al. (2017) further distinguished a local from a remote thermal effect by highlighting the important role played by the advection of offshore CHL-induced cold anomalies in the Benguela upwelling waters. The interplay of these mechanisms is regionally variable (Park et al., 2014). Despite the diversity of modelled responses, a consensus emerges on the first order effect of PLF on the ocean physics, which is to perturb the ocean thermal structure (Nakamoto et al., 2001; Murtuggude et al., 2002; Oschlies, 2004; Manizza et al., 2005, 2008; Anderson et al., 2007; Lengaigne et al., 2007; Gnanadesikan and Anderson, 2009; Löptien et al., 2009; Patara et al., 2012; Mignot et al., 2013; Hernandez et al., 2017). By trapping more heat at the ocean surface in eutrophic regions, such as coastal or equatorial upwellings areas, the presence of phytoplankton initially increases the surface warming. Confining heat at the surface leads to less heat penetrating in subsurface. In some cases, the advection and upwelling of subsurface cold anomalies can lead to remote cooling effects (Hernandez et al., 2017; Echevin et al., 2022). Dynamical readjustment in response to perturbations in thermal structure has also been shown to have a cooling effect, by increasing upwelling of cold water to the ocean surface (Manizza et al. 2005; Marzeion et al., 2005; Nakamoto et al., 2001; Löptien et al., 2009; Lengaigne et al., 2007; Park et al., 2014). Because these effects depend on upper ocean stratification, an important role is attributed to modelled seasonal deepening of the mixed layer as it determines the intensity of the underlying temperature anomaly and its vertical movement to the surface. In other terms, whatever the temporality of the causal chain, changes in the PLF representation are expected to both perturb the ocean heat uptake, and trigger perturbations of both the water column stratification and associated ocean dynamics.

b) This study: implications for N_2O budget uncertainties

Nitrous oxide (N_2O) is a major ozone-depleting substance (Ravishankara et al., 2009; Freing et al., 2012) and a potent greenhouse gas, whose global warming potential is 265-298 times that of CO_2 for a 100-year timescale (Myhre et al., 2013). The spatial coherence between marine productive areas and observed hot-spots of N_2O production leads to question the impact of an incomplete representation of the PLF on the simulated N_2O inventory. Recent observational studies highlight that N_2O production is high in low-oxygen tropical regions and cold upwelling waters (Arévalo-Martinez et al. 2018; 2020; Yang et al., 2020; Wilson et al., 2020). N_2O becomes increasingly saturated in surface waters of equatorial upwelling regions due to the upward advection of N_2O-rich waters (Arévalo-Martínez et al., 2017). Regions known to account for the most productive areas of the ocean spatially coincide with highest N_2O production: 64% of the annual N_2O flux occurs in the tropics, and 20% in coastal upwelling systems that occupy less than 3% of the ocean area (Yang et al., 2020).

Despite recent advances, a large range of uncertainties still surrounds oceanic N_2O emissions as large areas of both the open and coastal ocean remain undersampled by observations (Wilson et al., 2020). In particular, the paucity of observational data over key source regions contributes to increase uncertainties. The recent global budget of Tian et al. (2020) estimates natural sources from soils and oceans to contribute with up to 57% to the total N_2O emissions between 2007 and 2016, with the ocean flux reaching 3.4 (2.5–4.3) Tg N yr^{-1}. A large uncertainty range is associated to the ocean flux estimate, as it is based on outputs from only a small

number of global ocean-biogeochemical models. Very few climate models, even in the current CMIP6 generation, include emissions (and beforehand a complete representation of N cycling) of N_2O fluxes: only 4 out of the 26 Earth system models considered in Séférian et al. (2020) simulate marine N_2O emissions.

The last generation of Earth system models projects an enhanced ocean warming in response to climate change, which is in turn expected to increase upper-ocean stratification (Sallée et al., 2021) and to contribute to greater reductions in upper-ocean nitrate and subsurface oxygen ventilation (Kwiatkowski et al., 2020). Ocean warming and deoxygenation constitute two triggers of high-probability high-impact climate tipping points (Heinze et al., 2021) and are identified as two of the main environmental factors influencing marine N_2O distributions (IPCC, 2019; Hutchins and Capone, 2022). Through its expected impacts on the upper ocean stratification, the PLF representation could further change the oceanic N_2O source by modulating the mixing between N_2O-rich water and intermediate depths, perturbing the way N_2O-rich water reaches the air-sea interface (Freing et al., 2012).

Here we investigate how an incomplete representation of the PLF leads to uncertainties in N_2O projection in an up-to-date global ocean-biogeochemical model making up the current generation of Earth system models. Section 2 describes the numerical model and the set of simulations, as well as the existing options to consider CHL modulations of the incoming shortwave radiation. Section 3 presents the effect of an interactive PLF on the ocean heat content, associated ocean stratification and dynamics, and its feedback on marine N_2O inventory. Finally, Section 4 summarizes the main results, addresses their broader implications, and discusses the future work motivated by this study.

2. Methodology

a) Configuration of the global ocean-biogeochemical model

Recent projections of future N_2O emissions contributing to intercomparison projects like CMIP6 are still based on Earth system models with a low spatial resolution (Séférian et al., 2020). For sake of coherence with CMIP biogeochemical modelling efforts, in the following we use a global ocean-biogeochemical configuration of the NEMO-PISCESv2 model (Madec, 2008; Aumont et al., 2015) at 1° of horizontal resolution. This model corresponds to the oceanic component of CNRM-ESM2-1 (Séférian et al., 2019) and is one of the few CMIP6-class models that contributed to the Global N_2O budget (Tian et al., 2020). Our modelled ocean has 75 vertical levels and the first level is at 0.5 meter depth. Vertical levels are unevenly spaced with 35 levels being in the first 300 meters of depth. Atmospheric forcings of momentum, incoming radiation, temperature, humidity, and freshwater are provided to the ocean surface by bulk formulae following Large and Yeager (2009). Details on physical configuration are given in Berthet et al. (2019). Using an ocean-only configuration allows to isolate the local response induced by the PLF by not confounding it with potential inter-basin feedbacks acting through the atmosphere.

JRA55-do atmospheric reanalysis (Tsujino et al., 2018; Tsujino et al., 2020) provided the atmospheric forcings of the ocean. The global domain was first spun-up under preindustrial conditions during several hundred years ensuring that all fields approached a quasi-steady state. The historical evolution of atmospheric CO_2 and N_2O concentrations was prescribed since

188   1850. To avoid the warming jump between the end of the spin-up and the onset of the
189   reanalyses in 1958, the first 5 years of JRA55-do forcings were cycled, followed by the complete
190   period of JRA55-do atmospheric forcing from 1958 to 2018.

191

192   **b) Experimental design: three representations of the PLF**

193

194   The control simulation (hereafter REF) together with the spin-up both account for a fully
195   interactive PLF: the penetration of shortwave radiation into the ocean surface is constrained
196   by the CHL concentration ([CHL]) produced by the PISCESv2 biogeochemical component (Figure
197   S1, REF).

198

199   PISCESv2 (Pelagic Interactions Scheme for Carbon and Ecosystem Studies v2) is a 3D
200   biogeochemical model which simulates the lower trophic levels of marine ecosystems
201   (nanophytoplankton, diatoms, microzooplankton and mesozooplankton), the biogeochemical
202   cycles of carbon and of the main nutrients (phosphate, nitrogen, iron, and silicate) along the
203   75 levels of our numerical ocean. A comprehensive presentation of the model is found in
204   Aumont et al. (2015). PISCESv2 simulates prognostic 3D distributions of nanophytoplankton
205   and diatom concentrations. The evolution of phytoplankton biomasses is the net outcome of
206   growth, mortality, aggregation and grazing by zooplankton. Growth rate of phytoplankton
207   mainly depends on the length of the day, depths of the mixed layer and of the euphotic zone,
208   the mean residence time of the cells within the unlit part of the mixed layer and includes a
209   generic temperature dependency (Eppley, 1972). Nanophytoplankton growth depends on the
210   external nutrient concentrations in nitrogen and phosphate (Monod-like parameterizations of
211   N and P limitations), and on Fe limitation which is modeled according to a classical quota
212   approach. The production terms for diatoms are defined as for nanophytoplankton, except that
213   the limitation terms also include silicate.

214

215   Light absorption by phytoplankton depends on the waveband and on the species (Bricaud et
216   al., 1995). A simplified formulation of light absorption by the ocean is used in our experiments
217   to calculate both the phytoplankton light limitation in PISCESv2 and the oceanic heating rate
218   (Lengaigne et al., 2007). In this formulation, visible light is split into three wavebands: blue
219   (400–500 nm), green (500–600 nm) and red (600–700 nm); for each waveband, the CHL-
220   dependent attenuation coefficients, k_R, k_G and k_B, are derived from the formulation proposed
221   in Morel and Maritorena (2001):

222

223    $$k_{WLB} = \sum_{\lambda_1}^{\lambda_2}\big(k(\lambda) + \chi(\lambda)[\text{CHL}]^{e(\lambda)}\big) \hspace{3cm} (1)$$

224   where WLB means the wavelength band associated to red (R), green (G) or blue (B), and
225   bounded by the wavelengths λ_1 and λ_2 as detailed above. $k(\lambda)$ is the attenuation coefficient
226   for optically pure sea water. $\chi(\lambda)$ and $e(\lambda)$ are fitted coefficients which allows to determine
227   the attenuation coefficients due to chlorophyll pigments in sea water (Morel and Maritorena,
228   2001).

229
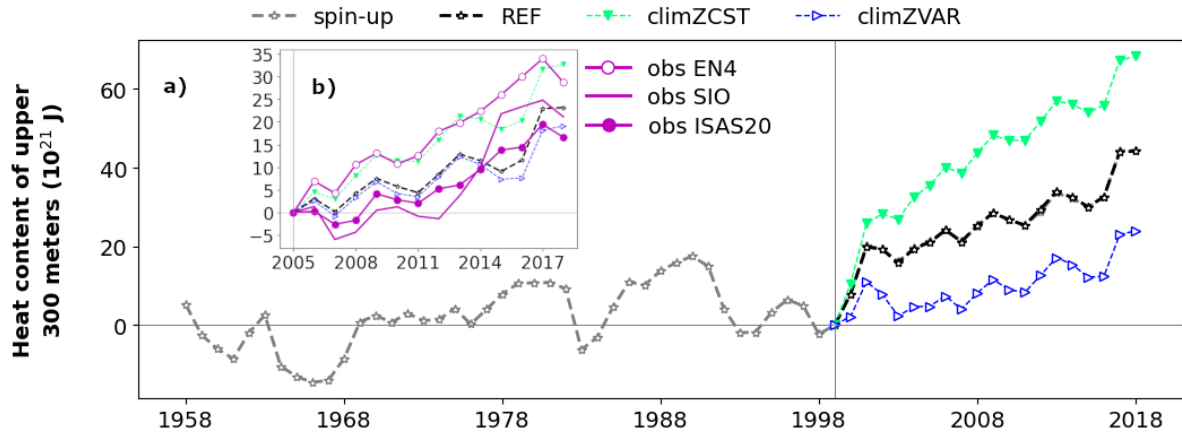
Figure 1: Modelled tropical [35°S-35°N] heat content of upper 300 m (OHC300; in ZJ) for each simulation described in Table 1: REF (black; empty stars), climZCST (green; full downward triangles) and climZVAR (blue; empty rightward triangles). In (a) final part of the spin-up has been added in gray to illustrate the branching protocol in year 1999, and OHC300 anomalies have been computed with respect to year 1999. Subplot (b) zooms over the Argo period to compare modelled tropical OHC300 anomalies with 3 in situ-based products (see section 2c).

At year 1999 two sensitivity experiments were branched off (Figure 1). Both simulations climZCST and climZVAR account for an incomplete and external PLF, as they consider an observed climatology of surface [CHL] from ESACCI (Valente et al., 2016) in order to compute the light penetration into sea water (Equation 1; Figure S1). These two simulations differ from each other by the "realism" of the vertical profile derived in each grid point from the surface value of the ESACCI CHL climatology to the level of light extinction (Table 1). climZCST uses constant profiles of CHL spreading uniformly in the vertical direction (Figure 2, b and d-f). climZVAR uses variable vertical profiles computed following Morel and Berthon (1989) (Figure 2, c and d-f). This set of simulations is representative of the several configurations used in the case of CMIP intercomparison project.

Table 1: Experimental set-up.

Simulation	Which CHL fields to interact with incoming shortwave radiation?	PLF nature
REF	uses directly the 3D CHL produced by the biogeochemical component	interactive
climZCST	uses the prescribed monthly climatology of ESACCI CHL with a constant vertical profile, equal to the value of the surface climatology up to the level of light extinction	incomplete
climZVAR	uses the prescribed monthly climatology of ESACCI CHL with a variable vertical profile, derived from the surface climatology following Morel and Berthon (1989)	incomplete

6

254 In climZCST and climZVAR, PISCESv2 prognostically simulates [CHL], a key component of
255 biogeochemical cycles, but feedback of CHL on physics (stratification, ocean heat content) is
256 determined by the externally prescribed [CHL] climatology. The CHL concentrations used for
257 radiation or for biogeochemical cycles are not consistent, and phytoplankton biomass
258 computed by the biogeochemical model does not affect the physical properties of the ocean
259 waters.

260

261 Consequences on the marine biogeochemical mean state of incomplete representations of the
262 PLF are assessed in the following by difference to the control run REF. This methodology allows
263 to evaluate how different levels of realisms and complexity in resolving bio-physical interactions
264 impact the physical and biogeochemical content of the modelled ocean. A complete
265 description of the marine N_2O parameterization used in this model is presented in the
266 supplementary material.
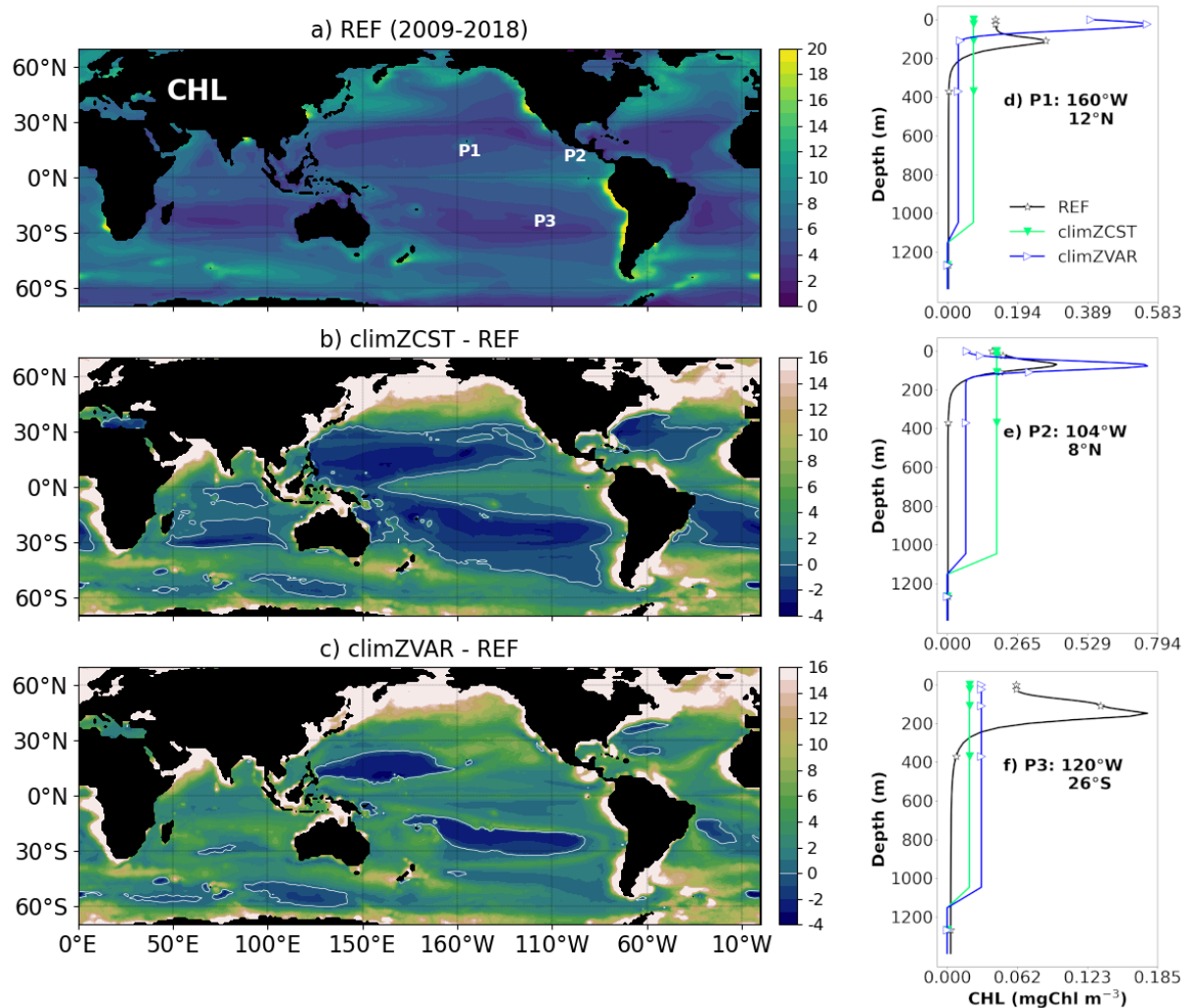
267
268 Figure 2: CHL concentration (mgCHL m^{-3}) interacting with the incoming shortwave radiation for
269 each numerical experiment (Table 1). Maps a-c) show annual means of the vertical sum over 0-
270 6000 m, a) as modelled over the 2009-2018 period for REF, and its differences with the external
271 CHL prescribed for b) climZCST and c) climZVAR experiments. Labels P1 to P3 on subplot a)
272 locate vertical profiles shown on subplots d-f).

273

c) Observations and analyses

Model results are compared with available observational-based gridded temperature and salinity datasets. Ocean heat content (OHC) of the upper 0-300 meter layer was inferred from three different products: i) the global objective analysis of subsurface temperature EN4 (Good et al., 2013), ii) the SIO product of the Scripps Institution of Oceanography (Roemmich anf Gilson, 2009), and iii) the ISAS20 optimal interpolation product released by Ifremer (Kolodziejczyk et al., 2019; Kolodziejczyk et al., 2021). While the SIO and ISAS20 products consider only Argo temperature and salinity profiles, the EN4 dataset considers all types of *in situ* profiles providing temperature and salinity (when available). These three *in situ*-based datasets are considered since 2005, the year the Argo coverage became sufficient to characterize the global ocean. Details on OHC computation are given in Llovel and Terray (2016) and Llovel et al. (2022). The authors also refer to cross-validations of OHC of deeper layers (0-700 m and 0-2000 m) against OHC anomalies from World Ocean Atlas 2009 (Levitus et al., 2012). A monthly climatology (1955-2012) of oceanic temperature from World Ocean Atlas 2013 version 2 (Locarnini et al., 2013) was used to evaluate modelled temperatures. Modelled O_2 was compared to the annual climatology of O_2 from World Ocean Atlas 2013 (Garcia et al., 2014) and modelled CHL was compared to the 3D monthly climatological global product estimated from merged satellite and hydrological data of Uitz et al. (2006). Modelled N_2O partial pressure difference across the air-sea interface (Dpn2o) was compared to the recent dataset of Dpn2o observations compiled by Yang et al. (2020).

In the following temporal means cover the last 10 years of simulations, from 2009 to 2018. In other analyses the whole simulated period is shown (1999-2018).

3. Results

a) Impact of PLF on the upper ocean heat content and dynamics

Meridional sections reveal that heat perturbations in response to changing CHL fields interacting with light are limited to the top 0-300 m layer of the ocean and predominantly affect the tropical area (Figure 3 and Figure S2, c-d).

The largest temperature anomalies are observed near the thermocline depth and reflect upper ocean warming and deepening of the thermocline in climZCST (Figure 3c), and cooling and shallowing of the thermocline in climZVAR (Figure 3d). In climZCST the ocean warming reflects large-scale patterns of a tropical CHL deficit compared to REF (Figure 2, b). Temperature differences are lower in the near-surface layer (0-50 m) than in the 50-300 m layer. This is expected as a result from weak stratification but also from simulations run with a forced atmosphere in which the temperature of the ocean surface layer is constrained by the atmospheric prescribed state.

When using an incomplete representation of the PLF, two contrasting trends of the upper ocean heat content (OHC) emerge compared to our control run REF (Figure 1a). Over the Argo period (2005-present) EN4 estimates of tropical OHC300 are in very good agreement with our warmest simulation climZCST (Figure 1b), while the two other dataproducts SIO and ISAS20 are

321 in better agreement with our control run REF and with climZVAR. The good accordance
322 between modeled OHC300 and observations is not a systematic feature of model-data
323 comparisons (Cheng et al., 2016; Liao et al., 2022). Moreover, non-negligible differences exist
324 among OHC dataproducts which are generally particularly strong in the upper 0-300 m layer
325 (Lyman et al., 2010; Liang et al., 2021). The spread between these products at the end of the
326 2005-2018 period (12.1 10^{21} J) is comparable to that of our numerical set (13.6 10^{21} J). The
327 modelled OHC in REF is in very good agreement with current global mean *in situ* observations
328 (Meyssignac et al., 2019; see their Figure 11) and with OHC anomalies derived from World
329 Ocean Atlas 2009 (Levitus et al., 2012). In accordance with these observations, our ocean-
330 biogeochemical model simulates a global mean increase of OHC over the 2006-2016 period of
331 order 40 10^{21} J for the upper 700 m, and of about 70 10^{21} J for the 0-2000 m layer.
332
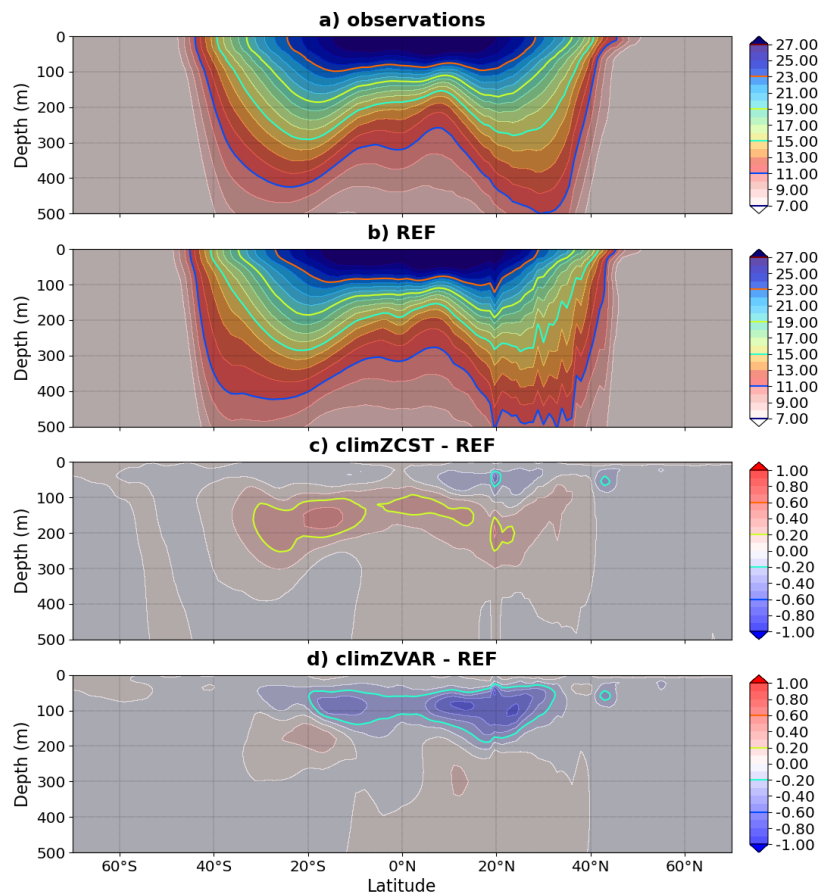
333
334

Figure 3: Mean 2009-2018 meridional section of temperature (°C) averaged over the whole
tropical band (0-360°E) for a) observations, b) REF and its differences with c) climZCST and d)
climZVAR.

335 Subsurface thermal anomalies develop rapidly (Figure S3) after branching of climZVAR and
336 climZCST in 1999. The dipole structure of the anomaly seen in climZCST reflects the surface
337 heat trapping in REF and the associated subsurface cooling (Figure S3, b). Indeed in climZCST
338 the vertically constant and weaker profiles of CHL trap less incoming shortwave than the CHL
339 maximum seen in REF between 0 and 100 m depth (Figure 2, d-f). The negative anomaly in
340 climZVAR suggests that the parameterization of Morel and Berthon (1989) contributes to
341 underestimate the ocean heat uptake (Figure S3, c and Figure S2, d) by comparison to REF. This

heat deficit results from the overestimation of the vertical integral of CHL over large areas of the tropical domain in climZVAR compared to REF (Figure 2, c). As a result, the energy associated with the incoming radiation is caught in surface waters without being distributed over the water column.

In both climZCST and climZVAR the subsurface temperature anomaly deepens progressively over the first six years of simulation as a result of vertical mixing (Figure S3). This evolution indicates that part of the OHC300 differences between simulations comes from the adjustment of climZCST and climZVAR to the spin-up mean state yielded by an interactive PLF. It can be expected that experiments having spin-ups run with different representations of the PLF, would give even stronger sensitivities than those highlighted in this study. The sensitivities of OHC300 to the PLF formulation evaluated here should be considered at the lower end of estimate of OHC discrepancies that may emerge from changing the PLF representation.

Prescribing a constant vertical profile of CHL (climZCST) to compute the penetration of the radiation into the ocean increases the OHC300 by more than 20 10^{21} J during the last two decades (1999-2018) compared to REF (Figure 1). This rise of OHC300 decreases the vertically-weighted sum of the tropical potential density of the upper 300 m at the end of the simulated period by 5 kg/m^3 compared to REF (Figure S4). The opposite trend (a reduced OHC300 compared to REF) is simulated with the same state-of-the-art CMIP6 ocean-biogeochemical model when considering a variable vertical profile of CHL (climZVAR). However Figure 1 highlights that the simulation using a consistent CHL for interacting with both incoming shortwave radiation and biogeochemical cyclings (REF) does not amplify one of these two trends, as climZCST and climZVAR surround REF. Average ranges of uncertainties associated with the PLF representation over the extended tropical domain (35°S-35°N) exceed 40 10^{21} J in terms of OHC300 (Figure 1), 4 meters for the thermocline depth and more than 9 kg/m^3 for the potential density perturbation (Figure S4).

Similar to OHC300, ranges of uncertainty for the OHC estimates of deeper layers (0-700 m and 0-2000 m) also slightly exceed 40 10^{21} J. Such uncertainty ranges are quite important as they are obtained by only changing the PLF representation in a single ocean-biogeochemical model. By comparison and in the context of OMIP protocols, Tsujino et al. (2020) give spreads between CMIP model estimates of the order of 50 10^{21} J for the OHC of the upper 700m after 20 years (please refer to their Figure 24, a-b). Regarding the OHC integrated over the 0-2000m layer, they report an inter-model spread between 50 and 100 10^{21} J, depending on the OMIP protocol considered (see their Figure 24, d-e). The OHC300 uncertainty of 40 10^{21} J triggered by the representation of the PLF in our set of simulations has a comparable order of magnitude than the current spread of multi-model estimations of OHC. The present study suggests that part of the OHC multi-model uncertainty in current climate models may be due to different representations of the phytoplankton-light interaction.

The heat and associated density perturbations also cause dynamical modifications of upper ocean currents (Figure 4). Absolute differences in upper ocean velocities (average between 0 and 300m depth) are between |0.05| and |0.6| cm/s with strongest differences along the equator revealing perturbations of the equatorial undercurrent (Figure 4, b and c). Circulation around the subtropical gyres is also impacted, in particular for the South Pacific subtropical gyre. These modifications of zonal and meridional dynamics spread over the entire tropical

389 latitudes, from 30°S to 30°N, strongly supporting the idea that heat perturbations induced by
390 different interactions between CHL and incoming shortwave cause non-negligible
391 modifications of the equatorial and tropical ocean dynamics.
392
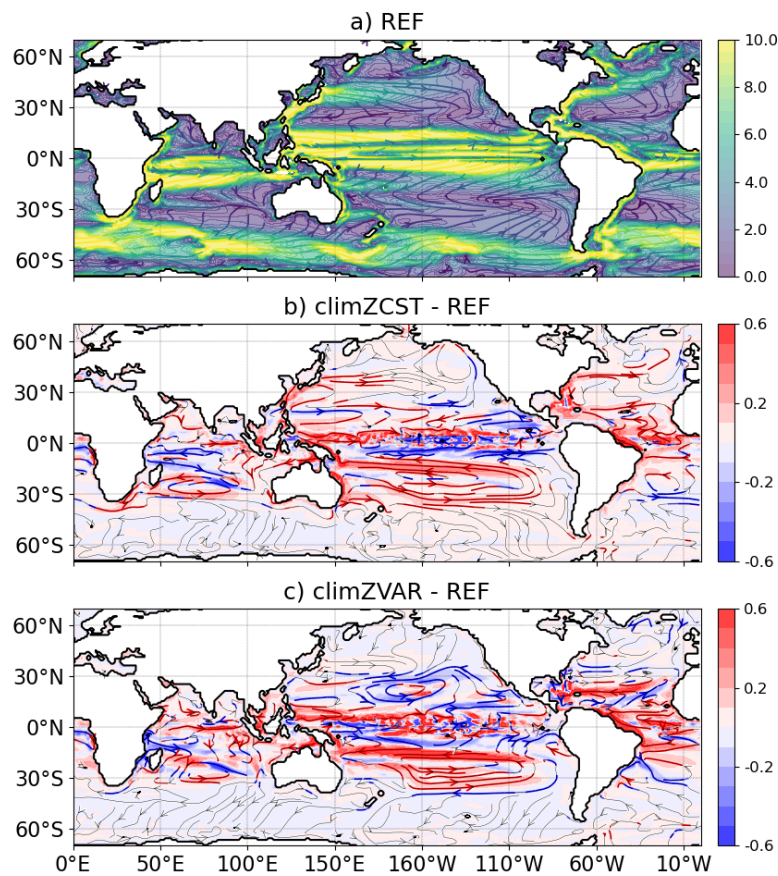
393
394 Figure 4: Annual mean speed (color; cm/s) and streamlines of oceanic currents between 0-300
395 m over the 2009-2018 period for a) REF, and its differences with b) climZCST and c) climZVAR.
396 In b-c) streamlines are colored when absolute speed are larger than 0.05 cm/s.

397
b) PLF impact on N_2O production
399
400 Perturbations of the annual pycnocline depth (Figure 5, a-c) highlight a vertical adjustment to
401 the heat (Figure S2) and subsequent large-scale dynamical anomalies (Figure 4). Variations of
402 the pycnocline integrate perturbations of both thermal and salinity stratifications. However, in
403 our simulations heat anomalies appear to drive perturbations and pycnocline depth anomalies
404 mainly reflect those of the thermocline. The cold anomaly dominating the tropical domain in
405 climZVAR (Figure S2, d) appears to be vertically redistributed, as it triggers an upward
406 displacement of the isopycnals (Figure 5, c). In contrast to the anomalies seen over most of the
407 tropical Pacific, a deepening of the isopycnals reaching up to 20 meters is modelled in both
408 South Pacific and Atlantic subtropical gyres in climZCST and climZVAR (Figure 5, b and c). Over
409 these subtropical gyres heat is redistributed along the vertical as the subsurface warm anomaly
410 dives. The subduction of these heat anomalies causes in turn a deepening of the pycnocline
411 (Figure 5, b and c). As stressed by Sweeney et al. (2005), small changes in CHL concentration
412 (Figure S5) may have important effects on the mixed layer depth in these subtropical gyres due

11

413 to low local wind speeds and low mixing conditions. This is thought to explain the large
414 sensitivity we observe in terms of pycnocline depth (Figure 5) and ocean heat content in these
415 regions. In line with their results, our set of simulations highlights that small CHL changes in low
416 productivity regions trigger a vertical redistribution of density anomalies affecting the
417 stratification.

418
419
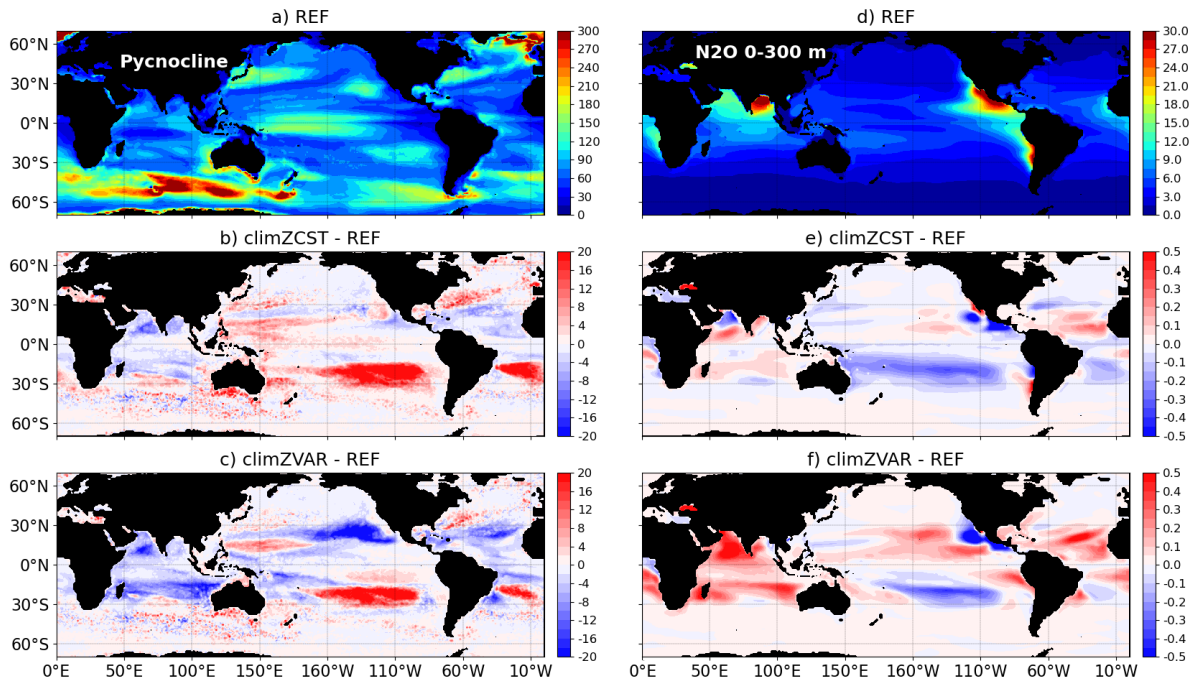
421 Figure 5: a-c) Depth of annual pycnocline (m) for 2009-2018 computed as the annual mean
422 depth of the maximum of the Brunt-Väisälä frequency $N^2(T, S)$ over the water column (Maes
423 and O Kane, 2014). d-f) Mean [N_2O] (μmolN/m^3) over the first 300 meters depth. For REF (upper
424 panel) and its mean-state differences with climZCST (middle panel) and climZVAR (bottom
425 panel).

426

427 Anomalies of N_2O concentration integrated over the first 300 meters of the water column
428 (Figure 5, e and f) are in good agreement with patterns of pycnocline anomalies over the tropics
429 (Figure 5, b and c). These comparable spatial structures attest that N_2O anomalies are driven
430 by perturbations of stratification in large parts of the tropical domain.

431

432 In the South Pacific subtropical gyre, the concomitance of i) an increased temperature (Figure
433 S2, c and d), ii) a reinforced transport (Figure 4, b and c) and iii) a weakened stratification
434 illustrated by a local deepening of the pycnocline (Figure 5, b and c), contributes to decrease
435 the N_2O concentration in both climZCST and climZVAR (Figure 5, e and f). In contrast, in the
436 South Indian Ocean and North tropical Atlantic the increase of N_2O concentration seems to be
437 mainly driven by the mean shoaling of the local pycnocline, as both regions exhibit contrasted
438 perturbations in terms of transport and temperature. Finally, in the North Pacific oxygen
439 minimum zone, the strong N_2O deficits in both climZCST and climZVAR compared to REF do not
440 respond to stratification and transport anomalies but are rather driven by a local rise of O_2
441 concentration (Figure S6). Considering an incomplete PLF contributes to overestimate the
442 oxygen concentration in this oxygen minimum zone and leads to a lack of local N_2O production.

443

444 The relationship between N_2O concentration and OHC300 in the Tropical Ocean is derived from
445 a linear regression for each of the three 20-years simulations (Figure 6). The resulting slopes
446 allow to identify three distinct tropical N_2O production pathways along time as a function of
447 the oceanic heat uptake: from 0.3 μmolN m^{-2} per ZJ for the most simplified PLF scenario
448 climZCST, to 1 μmolN m^{-2} per ZJ for climZVAR. The slope of the simulation with the higher level
449 of realism in terms of interactivity (REF) appears a solution between the two previous extremes,
450 as it increases its N_2O production by 0.8 μmolN m^{-2} per ZJ. Each of these N_2O production
451 pathways will translate into a different temporal evolution of the N_2O budget and hence future
452 climate. This result stresses the importance of having an interactive PLF in order to neither
453 overestimate nor underestimate the N_2O production projections due to a simplified
454 representation of the PLF.

455

456
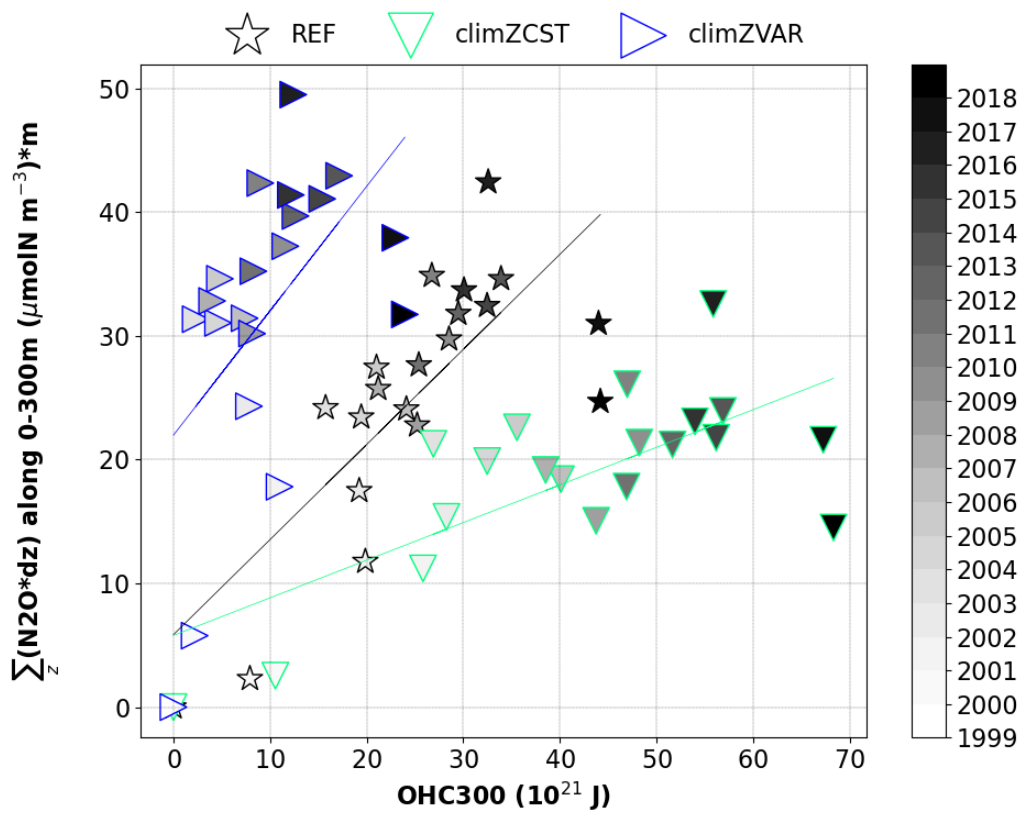
457 Figure 6: Annual N_2O inventory over the first 300 meters depth (μmolN/m^2/yr) as a function
458 of the annual OHC300 (ZJ/yr) and averaged over an extended tropical domain (35°S-35°N). All
459 points reflect anomalies compared to year 1999.

460

461 c) Impacts on oceanic N_2O emissions

462

463 By perturbing the OHC, the ocean dynamics and the N_2O production, the way PLF is modelled
464 has non-negligible consequences on Dpn2o and thus on N_2O emissions at the air-sea interface
465 (Figure 7). Because the atmospheric partial pressure of N_2O is identical among simulations,
466 differences in Dpn2o are driven by changes in surface N_2O concentration normalized by those
467 in N_2O solubility. Since solubility is mainly driven by temperature and because surface
468 temperature anomalies are very weak (Figure S3, c and d), we do not expect solubility

469 perturbations close to the surface. It results that spatial patterns of Dpn2o anomalies (Figure
470 7) reflect differences in surface N_2O concentration.

471

472 Compared to a scenario considering a fully interactive PLF (REF), an incomplete representation
473 of the PLF underestimates Dpn2o in all oxygen minimum zones of the northern hemisphere,
474 which are strong emission zones (Figure 7, c and d). Large Dpn2o anomalies of -2.5 natm
475 encompasses northern parts of the oxygen minimum zones of the Indian, Pacific and Atlantic
476 oceans and anomalies reach up to -5 natm locally. Consequently, climZCST and climZVAR
477 underestimate N_2O fluxes by more than 12% in these oxygen minimum regions compared to
478 REF. This result highlights that the representation of the PLF can be an important source of
479 uncertainty in modelling N_2O fluxes. As a matter of fact, the oceanic contribution to the recent
480 global N_2O budget by Tian et al. (2020) is based on only five global ocean-biogeochemical
481 models (as still only few models simulate marine N_2O emissions). These models have different
482 configurations of the PLF which adds considerable uncertainty to simulated marine N_2O
483 emissions.

484

485 In subtropical gyres, the strong and direct effect of temperature (Figure S2, c and d) on in-depth
486 N_2O concentration (Figure 5, e and f) is in line with Yang et al. (2020) who demonstrate that the
487 seasonality of Dpn2o in that regions is driven by a solubility regime. Both climZCST and
488 climZVAR overestimate Dpn2o in subtropical gyres of the South Pacific and South Atlantic
489 (Figure 7, c and d). This leads to an overestimation of the regional N_2O fluxes by 24% compared
490 to a simulation having a complete and interactive PLF representation (REF).

491
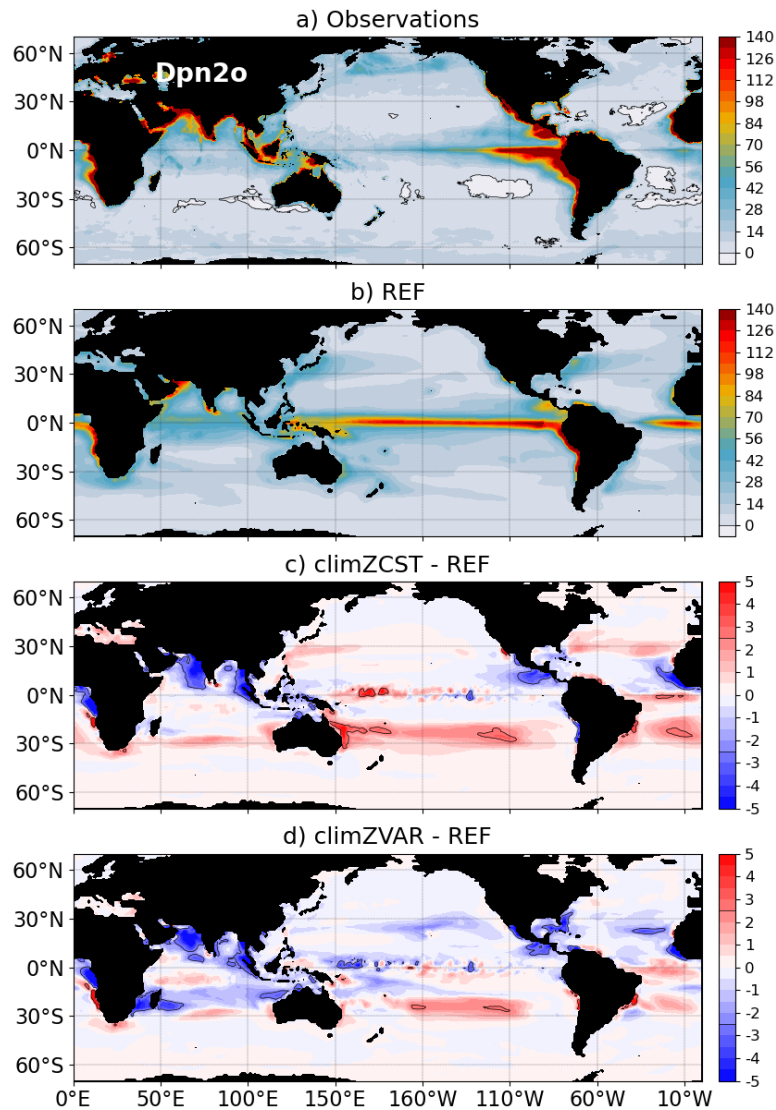
Figure 7: Mean sea-to-air Dpn2o (natm) computed from a) observations, b) REF over the 2009-2018 period, and its differences with c) climZCST and d) climZVAR compared to REF.

4. Discussion and conclusion

In this study we use the ocean component (including ocean physics, sea ice and marine biogeochemistry) of the global Earth system model CNRM-ESM2-1 which contributed to the last phase of the Coupled Model Intercomparison Project (CMIP6). Our ocean-biogeochemical model is one of the few currently able to represent an interactive phytoplankton-light feedback (PLF) by constraining the penetration of shortwave radiation into the ocean as a function of the CHL concentration produced by the biogeochemical model. Three simulations have been run at the horizontal resolution currently used for intercomparisons of Earth system models (1°). Analyses are based on differences between a control run with an interactive PLF (REF) and two experiments with an incomplete PLF (climZCST and climZVAR) using a prescribed CHL climatology to interact with the incoming solar radiation. Changing the approach to compute how CHL filters the light penetrating into the ocean highlights the consequences of using an interactive PLF.

Our results demonstrate that the approach commonly used to account for the impact of the phytoplankton on light penetration significantly interfers with upper ocean heat uptake (Figure 1), the associated dynamics (Figure 4) and stratification in the tropics (Figure 5, a-c). Our set of forced ocean-biogeochemical simulations reveals that marine production of nitrous oxide (N_2O) is sensitive to the representation of the PLF (Figure 5, d-f). The heat perturbations added to the uncertainty of modelled oceanic N_2O production and resulted in three N_2O production trajectories along time (Figure 6) that in turn trigger regional differences of Dpn2o and sea-air N_2O fluxes (Figure 7). Compared to an ocean model using a fully interactive PLF (REF), an incomplete PLF results in an overestimation of N_2O fluxes by up to 24% in the South Pacific and South Atlantic subtropical gyres, and a reduction by up to 12% in oxygen minimum zones of the northern hemisphere. Our results based on a model at CMIP6 state-of-the-art emphasize an overlooked important source of uncertainty in climate projections of marine N_2O production and in current estimations of the marine nitrous oxide budget.

In subtropical gyres of the southern Hemisphere which are regions of low productivity, small CHL changes have a strong and direct effect on temperature (Figure S2, c and d), transport (Figure 4, b and c) and local stratification (Figure 5, b and c). These concomittant effects result in a local decrease of N_2O concentrations in both experiments with a simplified PLF representation (climZCST and climZVAR).

In forced ocean simulations, atmospheric forcings constrain surface temperature, salinity and thus solubility. However, the N_2O concentration integrated over the upper 300 meters depth of the water column (Figure 5, e-f) showed differences with the control run that follow those of the in-depth temperature (Figure S2, c-d): in climZCST (climZVAR), a warmer (colder) tropical ocean leads to a decreased (an increased) N_2O concentration. Because higher marine greenhouse gas emissions will increase the temperature of the coupled atmosphere-ocean system, adding an interactive atmospheric component is expected to amplify the PLF-induced mean changes in marine N_2O concentration highlighted in this ocean-only numerical set (Park et al., 2014; Asselot et al., 2022).

Our results also question the reliability of current modelled estimates of the area and volume of oxygen minimum zones, as well as their trends in a future climate. The expansion rate of O_2-depleted waters still remains unclear and its controlling mechanisms are not yet fully understood and represented in today's models. Observation based assessments suggested that the ocean has already lost around 2% of the global marine oxygen since 1960 (Schmidtko et al., 2017). The expansion of oxygen minimum zones is expected to result in an increase of the volume of suboxic water and to have an impact on the production and decomposition of N_2O (Freing et al., 2012). Our set of simulations highlights that an incomplete representation of the PLF underestimates the expansion of oxygen-depleted waters over the 20 years of simulation in comparison to REF. In climZCST and climZVAR the global volume (0-1000 m) of hypoxic water with $[O_2]$ under 50 mmol m^{-3} is up to 2.3 10^{14} m^3 lower in 2018 compared to that of the control run REF. Thus an incomplete representation of the PLF might lead to an underestimation by 1.2 % of the modelled tropical volume of low-oxygenated waters after 20 years.

Recent regional studies demonstrated that the interactive PLF strongly affects upwelling systems of the South Pacific and Atlantic oceans (Hernandez et al., 2017; Echevin et al., 2021).

Coastal upwellings are known to be sites of high N_2O production with an annual N_2O flux amounting to approximately 20% of the global fluxes while these systems occupy less than 3% of the ocean area (Yang et al., 2020). However, in the present study main modelled perturbations are rather localized over oxygen minimum zones or subtropical gyres (Figure 5; Figure 7). While the latter regional studies were performed at horizontal resolutions compatible with the complex dynamics of coastal upwellings (from 10 km to about 28 km), the resolution of climate models (~1-degree of horizontal resolution) does not allow to resolve these dynamics. A step further would be to evaluate how the sensitivity of N_2O emission to the representation of the PLF depends on the horizontal resolution by running simulations at higher resolution with the same climate model. This would help to better determine how coastal upwelling systems may impact the modelled N_2O inventory through different PLF representations, as well as the associated modelled range of uncertainty.

Code availability

Sources for NEMO and PISCESv2 codes are available from https://forge.nemo-ocean.eu/nemo.

References

Anderson,W. G., A. Gnanadesikan, R. Hallberg, J. Dunne, and B. L. Samuels (2007), Impact of ocean color on the maintenance of the Pacific Cold Tongue, Geophys. Res. Lett., 34, L11609, doi:10.1029/2007GL030100.

Asselot, R., Lunkeit, F., Holden, P. B., & Hense, I. (2022). Climate pathways behind phytoplankton-induced atmospheric warming. Biogeosciences, 19(1), 223-239.

Aumont, O., Ethé, C., Tagliabue, A., Bopp, L., & Gehlen, M. (2015). PISCES-v2: An ocean biogeochemical model for carbon and ecosystem studies. Geoscientific Model Development, 8, 2465–2513.

Arévalo-Martinez, D. L., A. Kock, T. Steinhoff, P. Brandt, M. Dengler, T. Fischer, A. Körtzinger, and H. W. Bange (2017), Nitrous oxide during the onset of the Atlantic cold tongue, J. Geophys. Res. Oceans, 122, 171–184, doi:10.1002/2016JC012238

Arévalo-Martínez, D. L., Steinhoff, T., Brandt, P., Körtzinger, A., Lamont, T., Rehder, G., & Bange, H. W. (2019). N2O emissions from the northern Benguela upwelling system. Geophysical Research Letters, 46, 3317–3326. https://doi.org/10.1029/2018GL081648

Berthet, S., Séférian, R., Bricaud, C., Chevallier, M., Voldoire, A., & Ethé, C. (2019). Evaluation of an online grid-coarsening algorithm in a global eddy-admitting ocean biogeochemical model. Journal of Advances in Modeling Earth Systems, 11, 1759–1783. https://doi.org/10.1029/2019MS001644

605 **Bopp**, L., Resplandy, L., Orr, J. C., Doney, S. C., Dunne, J. P., Gehlen, M., Halloran, P., Heinze, C., Ilyina, T.,
606 Séférian, R., Tjiputra, J., and Vichi, M. (2013). Multiple stressors of ocean ecosystems in the 21st century:
607 projections with CMIP5 models, Biogeosciences, 10, 6225–6245, doi:10.5194/bg-10-6225-2013.
608
609 Bricaud, A., Babin, M., Morel, A., and Claustre, H.: Variability in the chlorophyll-specific absorption
610 coefficients of natural phytoplankton: analysis and parameterization, J. Geophys. Res., 100, 13321–13332,
611 1995.
612
613 **Cheng**, L., Trenberth, K. E., Palmer, M. D., Zhu, J., and Abraham, J. P.: Observed and simulated full-depth
614 ocean heat-content changes for 1970–2005, Ocean Sci., 12, 925–935, https://doi.org/10.5194/os-12-925-
615 2016, 2016.
616
617 **Cocco**, V., Joos, F., Steinacher, M., Frölicher, T. L., Bopp, L., Dunne, J., Gehlen, M., Heinze, C., Orr, J.,
618 Oschlies, A., Schneider, B., Segschneider, J., and Tjiputra, J. (2013). Oxygen and indicators of stress for
619 marine life in multi-model global warming projections, Biogeosciences, 10, 1849–1868, doi:10.5194/bg-10-
620 1849-2013.
621
622 **Echevin**, V., Hauschildt, J., Colas, F., Thomsen, S., & Aumont, O. (2021). Impact of chlorophyll shading on
623 the Peruvian upwelling system. Geophysical Research Letters, 48, e2021GL094429.
624 https://doi.org/10.1029/2021GL094429
625
626 Edwards, A. M., Wright, D. G., Platt, T. (2004) Biological heating effect of a band of phytoplankton. *Journal*
627 *of Marine Systems*, 49, 89-103. doi: 10.1016/j.jmarsys.2003.05.011.
628
629 Edwards, A. M., Platt, T., Wright, D. G. (2001) Biologically induced circulation at fronts. *Journal of*
630 *geophysical research*, 49, 89-103. doi: 10.1016/j.jmarsys.2003.05.011.
631
632 Eppley, R. W.: Temperature and phytoplankton growth in the sea, Fish. Bull., 70, 1063–1085, 1972.
633
634 **Freing**, A., D. W. R. Wallace, and H. W. Bange, 2012: Global oceanic production of nitrous oxide. Philos. Trans.
635 R. Soc. London Ser. B, **367**, 1245–1255.
636
637 **Garcia**, H. E., R. A. Locarnini, T. P. Boyer, J. I. Antonov, O.K. Baranova, M.M. Zweng, J.R. Reagan, D.R.
638 Johnson, (2014). World Ocean Atlas 2013, Volume 3: Dissolved Oxygen, Apparent Oxygen Utilization, and
639 Oxygen Saturation. S. Levitus, Ed., A. Mishonov Technical Ed.; NOAA Atlas NESDIS 75, 27 pp.
640
641 **Gildor**, H., and N. H. Naik (2005), Evaluating the effect of interannual variations of surface chlorophyll on
642 upper ocean temperature, J. Geophys. Res., 110, C07012, doi:10.1029/2004JC002779.
643
644 **Gnanadesikan**, A., and W. G. Anderson (2009), Ocean water clarity and the ocean general circulation in a
645 coupled climate model, J. Phys. Ocean., 39, 314–332.
646
647 **Good**, S. A., M. J. Martin and N. A. Rayner, (2013). EN4: quality controlled ocean temperature and salinity
648 profiles and monthly objective analyses with uncertainty estimates, Journal of Geophysical Research:
649 Oceans, doi:10.1002/2013JC009067
650
651 **Hajima**, T., Watanabe, M., Yamamoto, A., Tatebe, H., Noguchi, M. A., Abe, M., Ohgaito, R., Ito, A., Yamazaki,
652 D., Okajima, H., Ito, A., Takata, K., Ogochi, K., Watanabe, S., and Kawamiya, M. (2020). Development of the
653 MIROC-ES2L Earth system model and the evaluation of biogeochemical processes and feedbacks, Geosci.
654 Model Dev., 13, 2197–2244, https://doi.org/10.5194/gmd-13-2197-2020.
655
656 **Heinze**, C., T. Blenckner, H. Martins, D. Rusiecka, R. Döscher, M. Gehlen, N. Gruber, E. Holland, Ø. Hov, F.
657 Joos, J. B. R. Matthews, R. Rødven and S. Wilson (2021). The quiet crossing of ocean tipping points,
658 Proceedings of the National Academy of Sciences, 118 (9) e2008478118; DOI: 10.1073/pnas.2008478118

659

660 **Hernandez**, O., J. Jouanno, V. Echevin, and O. Aumont (2017), Modification of sea surface temperature by
661 chlorophyll concentration in the Atlantic upwelling systems, J. Geophys. Res. Oceans, 122, 5367–5389,
662 doi:10.1002/2016JC012330.

663

664 **Hutchins**, D.A., Capone, D.G. The marine nitrogen cycle: new developments and global change. Nat Rev
665 Microbiol (2022). https://doi-org.insu.bib.cnrs.fr/10.1038/s41579-022-00687-z

666

667 **Ilyina**, T., K. D. Six, J. Segschneider, E. Maier-Reimer, H. Li, and I. Núñez-Riboni (2013), Global ocean
668 biogeochemistrymodel HAMOCC: Model architecture and performance as component of the MPI-Earth
669 system model in different CMIP5 experimental realizations,J.Adv.Model.EarthSyst.,5, 287–315,
670 doi:10.1029/2012MS000178.

671

672 **IPCC**: Summary for Policymakers, in: IPCC Special Report on the Ocean and Cryosphere in a Changing
673 Climate, edited by: Pörtner,H.-O., Roberts, D.C., Masson-Delmotte, V., Zhai, P., Tignor, M., Poloczanska, E.,
674 Mintenbeck, K., Nicolai, M., Okem, A., Petzold, J., Rama, B., and Weyer, N., 2019.

675

676 **Ji**, Q., A. R. Babbin, A. Jayakumar, S. Oleynik, and B. B. Ward (2015), Nitrous oxide production by
677 nitrification and denitrification in the Eastern Tropical South Pacific oxygen minimum zone, Geophys. Res.
678 Lett., 42, 10,755–10,764, doi:10.1002/2015GL066853.

679

680 **Ji**, Q., Buitenhuis, E., Suntharalingam, P., Sarmiento, J. L., & Ward, B. B. (2018). Global nitrous oxide
681 production determined by oxygen sensitivity of nitrification and denitrification. Global Biogeochemical
682 Cycles, 32, 1790–1802. https://doi.org/10.1029/2018GB005887

683

684 **Kahru**, M., Leppaenen, J.-M., and Rud, O. (1993). Cyanobacterial blooms cause heating of the sea surface,
685 Mar. Ecol.-Prog. Ser., 101, 1–7.

686

687 **Kolodziejczyk**, N., W. Llovel, and E. Portela (2019). Interannual variability of upper ocean water masses as
688 inferred from Argo Array, Journal of Geophysical Research: Oceans. doi:10.1029/2018JC014866.

689

690 **Kolodziejczyk**, N., A. Prigent-Mazella and F. Gaillard (2021). ISAS temperature and salinity gridded fields.
691 SEANOE. https://doi.org/10.17882/52367

692

693 **Kortzinger**, A., Hedges, J. I., and Quay, P. D.: Redfield ratios revisited: removing the biasing effect of
694 anthropogenic CO2, Limnol. Oceanogr., 46, 964–970, 2001.

695

696 **Kwiatkowski**, L., Torres, O., Bopp, L., Aumont, O., Chamberlain, M., Christian, J. R., Dunne, J. P., Gehlen, M.,
697 Ilyina, T., John, J. G., Lenton, A., Li, H., Lovenduski, N. S., Orr, J. C., Palmieri, J., Santana-Falcón, Y.,
698 Schwinger, J., Séférian, R., Stock, C. A., Tagliabue, A., Takano, Y., Tjiputra, J., Toyama, K., Tsujino, H.,
699 Watanabe, M., Yamamoto, A., Yool, A., and Ziehn, T.: Twenty-first century ocean warming, acidification,
700 deoxygenation, and upper-ocean nutrient and primary production decline from CMIP6 model projections,
701 Biogeosciences, 17, 3439–3470, https://doi.org/10.5194/bg-17-3439-2020, 2020.

702

703 **Lam**, P., and M. Kuypers (2011). Microbial Nitrogen Cycling Processes in Oxygen Minimum Zones, Annual
704 Review of Marine Science 3:1, 317-345, doi:10.1146/annurev-marine-120709-142814

705
706 **Large**, W. G., and S. Yeager (2009). The global climatology of an interannually varying air-sea ux data set,
707 Clim. Dyn., 33, 341–364, doi:10.1007/s00382-008-0441-3.

708

709 **Lengaigne**, M., G. Madec, L. Bopp, C. Menkes, O. Aumont, and P. Cadule (2009). Bio-physical feedbacks in
710 the Arctic Ocean using an Earth system model, Geophys. Res. Lett., 36, L21602,
711 doi:10.1029/2009GL040145.

712

713 **Lengaigne**, M., Menkes, C., Aumont, O. et al. Influence of the oceanic biology on the tropical Pacific climate
714 in a coupled general circulation model. Clim. Dyn., 28, 503–516 (2007). https://doi.org/10.1007/s00382-
715 006-0200-2

717 **Levitus**, S., J. I. Antonov, T. P. Boyer, O. K. Baranova, H. E. Garcia, R. A. Locarnini, A.V. Mishonov, J. R.
718 Reagan, D. Seidov, E. S. Yarosh, M. M. Zweng, (2012): World Ocean heat content and thermosteric sea level
719 change (0-2000 m) 1955-2010. Geophys. Res. Lett. , 39, L10603, doi:10.1029/2012GL051106

721 **Liang**, X., Liu, C. R., Ponte, M., and Chambers, D. P. (2021). A Comparison of the Variability and Changes in
722 Global Ocean Heat Content from Multiple Objective Analysis Products During the Argo Period, J. Climate,
723 34(19), 7875–7895, https://doi.org/10.1175/JCLID-20-0794.1.

725 **Llovel**, W. and L. Terray (2016). Observed southern upper-ocean warming over 2005–2014 and associated
726 mechanisms, Environ. Res. Lett., 11, 124023.

728 **Llovel**, W., N. Kolodziejczyk, S. Close, T. Penduff, J.-M. Molines and L. Terray (2022). Imprint of intrinsic
729 ocean variability on decadal trends of regional sea level and ocean heat content using synthetic profiles,
730 Environ. Res. Lett., 17, 044063.

732 **Locarnini**, R. A., A. V. Mishonov, J. I. Antonov, T. P. Boyer, H. E. Garcia, O. K. Baranova, M. M. Zweng, C. R.
733 Paver, J. R. Reagan, D. R. Johnson, M. Hamilton, and D. Seidov, (2013). World Ocean Atlas 2013, Volume 1:
734 Temperature. S. Levitus, Ed., A. Mishonov Technical Ed.; NOAA Atlas NESDIS 73, 40 pp.

736 **Löptien**, U., C. Eden, A. Timmermann, and H. Dietze (2009), Effects of biologically induced differential
737 heating in an eddy-permitting coupled ocean-ecosystem model, J. Geophys. Res., 114, C06011,
738 doi:10.1029/2008JC004936.

739 **Lyman**, J., Good, S., Gouretski, V. et al. Robust warming of the global upper ocean. Nature **465,** 334–337
740 (2010). https://doi.org/10.1038/nature09043

741 **Madec**, G. (2008). Nemo ocean engine. Note du Pôle de modélisation de l'Institut Pierre-Simon Laplace, 27,
742 1–217.

744 **Maes**, C., and T. J. O'Kane (2014), Seasonal variations of the upper ocean salinity stratification in the
745 Tropics, J. Geophys. Res. Oceans, 119, 1706–1722, doi:10.1002/2013JC009366.

747 **Manizza**, M., C. Le Quéré, A. J. Watson, and E. T. Buitenhuis (2005), Bio-optical feedbacks among
748 phytoplankton, upper ocean physics and sea-ice in a global model, Geophys. Res. Lett., 32, L05603,
749 doi:10.1029/2004GL020778.

751 **Manizza**, M., C. Le Quéré, A. J. Watson, and E. T. Buitenhuis (2008), Ocean biogeochemical response to
752 phytoplankton-light feedback in a global model, J. Geophys. Res., 113, C10010, doi:10.1029/2007JC004478.

754 **Martinez-Rey**, J., Bopp, L., Gehlen, M., Tagliabue, A., and Gruber, N.: Projections of oceanic N_2O emissions
755 in the 21st century using the IPSL Earth system model, Biogeosciences, 12, 4133–4148,
756 https://doi.org/10.5194/bg-12-4133-2015, 2015.

758 **Marzeion**, B., Timmermann, A., Murtugudde, R., & Jin, F. (2005). Biophysical Feedbacks in the Tropical
759 Pacific, Journal of Climate, 18(1), 58-70.

761 **Meyssignac** B, Boyer T, Zhao Z, Hakuba MZ, Landerer FW, Stammer D, Köhl A, Kato S, L'Ecuyer T, Ablain M,
762 Abraham JP, Blazquez A, Cazenave A, Church JA, Cowley R, Cheng L, Domingues CM, Giglio D, Gouretski V,
763 Ishii M, Johnson GC, Killick RE, Legler D, Llovel W, Lyman J, Palmer MD, Piotrowicz S, Purkey SG, Roemmich
764 D, Roca R, Savita A, von Schuckmann K, Speich S, Stephens G, Wang G, Wijffels SE and Zilberman N (2019)

765 Measuring Global Ocean Heat Content to Estimate the Earth Energy Imbalance. Front. Mar. Sci. 6:432. doi:
766 10.3389/fmars.2019.00432
767
768 **Mignot**, J., D. Swingedouw, J. Deshayes, O. Marti, C. Talandier, R. Séférian, M. Lengaigne, G. Madec (2013).
769 On the evolution of the oceanic component of the IPSL climate models from CMIP3 to CMIP5: A mean state
770 comparison, Ocean Modelling, Volume 72, Pages 167-184, ISSN 1463-5003,
771 https://doi.org/10.1016/j.ocemod.2013.09.001.
772
773 **Morel** A (1988) Optical modeling of the upper ocean in relation to its biogenous matter content (Case I
774 waters). J Geophys Res 93:10749–10768
775
776 **Morel**, A. and J.-F. Berthon, 1989 : Surface pigments, algal biomass profiles, and potential production of the
777 euphotic layer : Relationships reinvestigated in view of remote-sensing applications. Limnol. Oceanogr.,
778 34(8), 1545–1562.
779
780 **Morel** A, and Maritorena S (2001) Bio-optical properties of oceanic waters: a reappraisal. J Geophys Res
781 106:7163–7180
782
783 **Murtugudde**, R., Beauchamp, J., McClain, C. R., Lewis, M., & Busalacchi, A. J. (2002). Effects of Penetrative
784 Radiation on the Upper Tropical Ocean Circulation, Journal of Climate, 15(5), 470-486.
785
786 **Myhre**, G., D. Shindell, F.-M. Bréon, W. Collins, J. Fuglestvedt, J. Huang, D. Koch, J.-F. Lamarque, D. Lee, B.
787 Mendoza, T. Nakajima, A. Robock, G. Stephens, T. Takemura and H. Zhang, (2013). Anthropogenic and
788 Natural Radiative Forcing. In: Climate Change 2013: The Physical Science Basis. Contribution of Working
789 Group I to the Fifth Assessment Report of the Intergovernmental Panel on Climate Change [Stocker, T.F., D.
790 Qin, G.-K. Plattner, M. Tignor, S.K. Allen, J. Boschung, A. Nauels, Y. Xia, V. Bex and P.M. Midgley (eds.)].
791 Cambridge University Press, Cambridge, United Kingdom and New York, NY, USA.
792
793 **Nakamoto**, S., S. P. Kumar, J. M. Oberhuber, J. Ishizaka, K. Muneyama, and R. Frouin (2001), Response of
794 the equatorial Pacific to chlorophyll pigment in a mixed layer isopycnical ocean general circulation model,
795 Geophys. Res. Lett., 28, 2021– 2024.
796
797 **Oschlies**, A. (2004), Feedbacks of biotically induced radiative heating on upper-ocean heat budget,
798 circulation, and biological production in a coupled ecosystem-circulation model, J. Geophys. Res., 109,
799 C12031, doi:10.1029/2004JC002430.
800
801 **Park**, JY., Kug, JS., Seo, H. et al. Impact of bio-physical feedbacks on the tropical climate in coupled and
802 uncoupled GCMs. Clim Dyn **43**, 1811–1827 (2014). https://doi.org/10.1007/s00382-013-2009-0
803
804 **Patara**, L., Vichi, M., Masina, S. et al. Global response to solar radiation absorbed by phytoplankton in a
805 coupled climate model. Clim Dyn **39**, 1951–1968 (2012). https://doi.org/10.1007/s00382-012-1300-9
806
807 **Ravishankara**, A. R., J. S. Daniel, and R. W. Portmann, 2009: Nitrous oxide (N2O): The dominant ozone-
808 depleting substance emitted in the 21st century. Science, **326**, 123–125.
809
810 **Roemmich**, D., and J. Gilson, 2009: The 2004–2008 mean and annual cycle of temperature, salinity, and
811 steric height in the global ocean from the Argo Program. Prog. Oceanogr., 82,
812 81–100, https://doi.org/10.1016/j.pocean.2009.03.004.
813
814 **Sallée**, JB., Pellichero, V., Akhoudas, C. *et al.* Summertime increases in upper-ocean stratification and
815 mixed-layer depth. Nature 591**,** 592–598 (2021). https://doi.org/10.1038/s41586-021-03303-x
816
817 **Schmidtko**, S., Stramma, L. & Visbeck, M. Decline in global oceanic oxygen content during the past five
818 decades. Nature 542, 335–339 (2017).

819

820 **Séférian**, R., Berthet, S., Yool, A. et al. Tracking Improvement in Simulated Marine Biogeochemistry
821 Between CMIP5 and CMIP6. Curr Clim Change Rep **6,** 95–119 (2020). https://doi.org/10.1007/s40641-020-
822 00160-0

823

824 **Séférian**, R., Nabat, P., Michou, M., Saint-Martin, D., Voldoire, A., Colin, J., et al (2019). Evaluation of CNRM
825 Earth-System model, CNRM-ESM2-1: role of Earth system processes in present-day and future climate.
826 Journal of Advances in Modeling Earth Systems, 11. https://doi.org/10.1029/2019MS001791

827

828 **Sweeney**, C, Gnanadesikan, A., Griffies, S. M., Harrison, M. J., Rosati, A. J., & Samuels, B. L. (2005). Impacts
829 of Shortwave Penetration Depth on Large-Scale Ocean Circulation and Heat Transport, Journal of Physical
830 Oceanography, 35(6), 1103-1119.

831

832 **Takahashi**, T., Broecker, W. S., and Langer, S.: Redfield ratio based on chemical data from isopycnal
833 surfaces, J. Geophys. Res., 90, 6907–6924, 1985.

834

835 **Tian**, H., Xu, R., Canadell, J.G., R. L. Thompson, W. Winiwarter, P. Suntharalingam, E. A. Davidson, P. Ciais, R.
836 B. Jackson, G. Janssens-Maenhout, M. J. Prather, P. Regnier, N. Pan, S. Pan, G. Peters, H. Shi, F. N. Tubiello,
837 S. Zaehle, F. Zhou, A. Arneth, G. Battaglia, S. Berthet, L. Bopp, A. F. Bouwman, E. T. Buitenhuis, J. Chang,
838 Martyn P. Chipperfield, S. R.S. Dangal, E. Dlugokencky, J. Elkins, Bradley D. Eyre, B. Fu, B. Hall, A. Ito, F. Joos,
839 P. B. Krummel, A. Landolfi, G. G. Laruelle, R. Lauerwald, W. Li, S. Lienert, T. Maavara, M. MacLeod, D. B.
840 Millet, S. Olin, P. K. Patra, R. G. Prinn, P. A. Raymond, D. J. Ruiz, Guido R. van der Werf, N. Vuichard, J.
841 Wang, R. Weiss, K. C. Wells, C. Wilson, J. Yang and Y. Yao (2020). A comprehensive quantification of global
842 nitrous oxide sources and sinks. Nature 586, 248–256.
843 https://doi.org/10.1038/s41586-020-2780-0.

844

845 **Tiano**, L., E. Garcia-Robledo, T. Dalsgaard, A. H. Devol, B. B. Ward, O. Ulloa, D. E. Canfield, N. P. Revsbech
846 (2014). Oxygen distribution and aerobic respiration in the north and south eastern tropical Pacific oxygen
847 minimum zones. Deep Sea Research Part I: Oceanographic Research Papers, Volume 94, Pages 173-183,
848 https://doi.org/10.1016/j.dsr.2014.10.001.

849

850 **Timmermann**, A., and F.-F. Jin, 2002. Phytoplankton influences on tropical climate, Geophys. Res. Lett.,
851 29(23), 2104, doi:10.1029/2002GL015434.

852

853 **Tsujino**, H., Urakawa, S., Nakano, H., Small, R. J., Kim, W. M., Yeager, S. G., Danabasoglu, G., Suzuki, T.,
854 Bamber J. L., Bentsen, M., Böning, C. W., Bozec, A., Chassignet, E. P., Curchitser, E., Boeira Dias, F., Durack,
855 P. J., Griffies, S. M., Harada, Y., Ilicak, M., Josey, S. A., Kobayashi, C., Kobayashi, S., Komuro, Y., Large, W. G.,
856 Le Sommer, J., Marsland, S. J., Masina, S., Scheinert, M., Tomita, H., Valdivieso, M., and Yamazaki, D.
857 (2018). JRA-55 based surface dataset for driving ocean–sea-ice models (JRA55-do), Ocean Model., 130, 79–
858 139, https://doi.org/10.1016/j.ocemod.2018.07.002.

859

860 **Tsujino**, H., Urakawa, L. S., Griffies, S. M., Danabasoglu, G., Adcroft, A. J., Amaral, A. E., Arsouze, T., Bentsen,
861 M., Bernardello, R., Böning, C. W., Bozec, A., Chassignet, E. P., Danilov, S., Dussin, R., Exarchou, E., Fogli, P.
862 G., Fox-Kemper, B., Guo, C., Ilicak, M., Iovino, D., Kim, W. M., Koldunov, N., Lapin, V., Li, Y., Lin, P., Lindsay,
863 K., Liu, H., Long, M. C., Komuro, Y., Marsland, S. J., Masina, S., Nummelin, A., Rieck, J. K., Ruprich-Robert, Y.,
864 Scheinert, M., Sicardi, V., Sidorenko, D., Suzuki, T., Tatebe, H., Wang, Q., Yeager, S. G., and Yu, Z. (2020).
865 Evaluation of global ocean–sea-ice model simulations based on the experimental protocols of the Ocean
866 Model Intercomparison Project phase 2 (OMIP-2), Geosci. Model Dev., 13, 3643–3708,
867 https://doi.org/10.5194/gmd-13-3643-2020, 2020.

868

869 Uitz, J., Claustre, H., Morel, A., and Hooker, S. B. (2006), Vertical distribution of phytoplankton communities
870 in open ocean: An assessment based on surface chlorophyll, *J. Geophys. Res.*, 111, C08005,
871 doi:10.1029/2005JC003207.

872

873

874 ~~Wanninkhof, R. (1992). Relationship between wind speed and gas exchange over the ocean, J. Geophys.~~
875 ~~Res., 97, 7373–7382, doi:10.1029/92JC00188.~~
876
877 ~~Wanninkhof, Rik, (2014), Relationship between wind speed and gas exchange over the ocean revisited,~~
878 ~~Limnol. Oceanogr. Methods, 12, doi:10.4319/lom.2014.12.351.~~
879
880 ~~Yang, S., B. X. Chang, M. J. Warner, T. S. Weber, A. M. Bourbonnais, A. E. Santoro, A. Kock, R. E. Sonnerup, J.~~
881 ~~L. Bullister, S. T. Wilson and D. Bianchi (2020). Global reconstruction reduces the uncertainty of oceanic~~
882 ~~nitrous oxide emissions and reveals a vigorous seasonal cycle, Proceedings of the National Academy of~~
883 ~~Sciences, 117 (22) 11954-11960; DOI: 10.1073/pnas.1921914117~~
884 Valente, A, Sathyendranath, S, Brotas, V, Groom, S, Grant, M, Taberner, M, Antoine, D, Arnone, R, Balch, W,
885 Barker, K, Barlow, R, Bélanger, S, Berthon, JF, Besiktepe, S, Brando, V, Canuti, E, Chavez, F, Claustre, H,
886 Crout, R, Frouin, R, Garcìa-Soto, C, Gibb, SW, Gould, R, Hooker, S, Kahru, M, Klein, H, Kratzer, S, Loisel, H,
887 McKee, D, Mitchell, BG, Moisan, T, Muller-Karger, F., O'Dowd, L, Ondrusek, M, Poulton, A, Repecaud, M,
888 Smyth, T, Sosik, HM, Twardowski, M, Voss, K, Werdell, J, Wernand, M, Zibordi, G (2016) A compilation of
889 global bio-optical in situ data for ocean-colour satellite applications. Earth Syst. Sci. Data, 8, 235–252, doi:
890 10.5194/essd-8-235-2016
891
892 Wanninkhof, R. (1992). Relationship between wind speed and gas exchange over the ocean, J. Geophys.
893 Res., 97, 7373–7382, doi:10.1029/92JC00188.
894
895 Wanninkhof, Rik, (2014), Relationship between wind speed and gas exchange over the ocean revisited,
896 Limnol. Oceanogr. Methods, 12, doi:10.4319/lom.2014.12.351.
897
898 Weiss, R. F., and B. A. Price (1980). Nitrous oxide solubility in water and seawater Marine Chemistry,
899 Volume 8, Issue 4, Pages 347-359; DOI: 10.1016/0304-4203(80)90024-9
900
901 Wilson, S. T., Al-Haj, A. N., Bourbonnais, A., Frey, C., Fulweiler, R. W., Kessler, J. D., Marchant, H. K., Milucka,
902 J., Ray, N. E., Suntharalingam, P., Thornton, B. F., Upstill-Goddard, R. C., Weber, T. S., Arévalo-Martínez, D.
903 L., Bange, H. W., Benway, H. M., Bianchi, D., Borges, A. V., Chang, B. X., Crill, P. M., del Valle, D. A., Farías, L.,
904 Joye, S. B., Kock, A., Labidi, J., Manning, C. C., Pohlman, J. W., Rehder, G., Sparrow, K. J., Tortell, P. D.,
905 Treude, T., Valentine, D. L., Ward, B. B., Yang, S., and Yurganov, L. N.: Ideas and perspectives: A strategic
906 assessment of methane and nitrous oxide measurements in the marine environment, Biogeosciences, 17,
907 5809–5828, https://doi.org/10.5194/bg-17-5809-2020, 2020.
908
909 Yang, S., B. X. Chang, M. J. Warner, T. S. Weber, A. M. Bourbonnais, A. E. Santoro, A. Kock, R. E. Sonnerup, J.
910 L. Bullister, S. T. Wilson and D. Bianchi (2020). Global reconstruction reduces the uncertainty of oceanic
911 nitrous oxide emissions and reveals a vigorous seasonal cycle, Proceedings of the National Academy of
912 Sciences, 117 (22) 11954-11960; DOI: 10.1073/pnas.1921914117
913